RESEARCH ARTICLE

Indirect printing of hierarchical patient-specific scaffolds for meniscus tissue engineering

João B. Costa[1,2,3] · Joana Silva-Correia[1,2] · Sandra Pina[1,2] · Alain da Silva Morais[1,2] · Sílvia Vieira[1,2] · Hélder Pereira[1,2,4,5] · João Espregueira-Mendes[1,2,6,7,8] · Rui L. Reis[1,2,3] · Joaquim M. Oliveira[1,2,3]

Abstract

The complex meniscus tissue plays a critical role in the knee. The high susceptibility to injury has led to an intense pursuit for better tissue engineering regenerative strategies, where scaffolds play a major role. In this study, indirect printed hierarchical multilayered scaffolds composed by a silk fibroin (SF) upper layer and an 80/20 (w/w) ratio of SF/ionic-doped β-tricalcium phosphate (TCP) bottom layer were developed. Furthermore, a comparative analysis between two types of scaffolds produced using different SF concentrations, i.e., 8% (w/v) (Hi8) and 16% (w/v) (Hi16) was performed. In terms of architecture and morphology, the produced scaffolds presented homogeneous porosity in both layers and no differences were observed when comparing both scaffolds. A decrease in terms of mechanical performance of the scaffolds was observed when SF concentration decreased from 16 to 8% (w/v). Hi16 revealed a static compressive modulus of 0.66 ± 0.05 MPa and dynamical mechanical properties ranging from 2.17 ± 0.25 to 3.19 ± 0.38 MPa. By its turn, Hi8 presented a compressive modulus of 0.27 ± 0.08 MPa and dynamical mechanical properties ranging from 1.03 ± 0.08 MPa to 1.56 ± 0.13 MPa. In vitro bioactivity studies showed formation of apatite crystals onto the surface of Hi8 and Hi16 bottom layers. Human meniscus cells (hMCs) and human primary osteoblasts were cultured separately onto the top layer (SF8 and SF16) and bottom layer (SF8/TCP and SF16/TCP) of the hierarchical scaffolds Hi8 and Hi16, respectively. Both cell types showed good adhesion and proliferation as denoted by the live/dead staining, Alamar Blue assay and DNA quantification analysis. Subcutaneous implantation in mice revealed weak inflammation and scaffold's integrity. The hierarchical indirect printed SF scaffolds can be promising candidate for meniscus TE scaffolding applications due their suitable mechanical properties, good biological performance and possibility of being applied in a patient-specific approach.

Keywords Patient-specific · Indirect printing · Hierarchical · Silk fibroin · Enzymatic-cross-linking · Meniscus

✉ Joaquim M. Oliveira
miguel.oliveira@i3bs.uminho.pt

1 3B´s Research Group, I3Bs – Research Institute on Biomaterials, Biodegradables and Biomimetics, University of Minho, Headquarters of the European Institute of Excellence on Tissue Engineering and Regenerative Medicine, AvePark, Zona Industrial da Gandra, 4805-017 Barco Gmr, Portugal

2 ICVS/3B's - PT Government Associate Laboratory, Braga/Guimarães, Portugal

3 The Discoveries Centre for Regenerative and Precision Medicine, Headquarters at University of Minho, Avepark, 4805-017 Barco, Guimarães, Portugal

4 Ripoll y De Prado Sports Clinic: Murcia-Madrid FIFA Medical Centre of Excellence, Murcia, Spain

5 Orthopedic Department Centro Hospitalar Póvoa de Varzim, Vila do Conde, Portugal

6 Clínica do Dragão, Espregueira-Mendes Sports Centre, FIFA Medical Centre of Excellence, Porto, Portugal

7 Dom Henrique Research Centre, Porto, Portugal

8 Orthopedic Department, University of Minho, Braga, Portugal

🖄 Springer

Introduction

The important role of meniscus in the knee and its high susceptibility to injury led to an intensification of the interest and awareness in this field from the scientific and medical community [1]. Current treatment options for meniscal injuries rely into three strategies: (1) non-operative, (2) meniscectomy and (3) meniscal repair. The decision for the most suitable strategy in each case depends on several factors such as patient age, location of tear and type and size of tear. For older patients, there are already some evidences proving that it is better to proceed with a non-operative approach rather than meniscectomy, since partial meniscectomy only showed reasonable outcomes when the peripheral meniscal rim is intact [2]. Furthermore, there has been an increasing number of meniscus repairs being performed by arthroscopically assisted inside-out techniques (CPT codes 29882 and 29883) over the past 7 years, suggesting that this strategy has been preferentially performed over meniscectomies in case of younger patients [3]. In sum, new and more effective approaches for meniscus repair are needed as there is still space for improvements of the current used techniques. Several strategies have already been proposed, but only few of them have been shown to be effective [4]. Tissue engineering (TE) approaches have been applied in the orthopedic field, namely for meniscus regeneration showing very promising preclinical results and high potential for clinical applications in a near future [5]. Associated to advances in engineering of scaffolds, patient specificity is becoming an important requisite in many TE approaches and orthopedic applications, including the treatment of meniscus lesions [6]. These can allow reducing the overall procedure costs, minimizing the surgical time, and more importantly address the need for enhancing implant anchorage for ultimately achieving a better biomechanical stability and biofunctionality [7]. By means of combining reverse engineering with a rapid prototyping technique, it is possible to print custom-made scaffolds with appropriate size and shape. In terms of biocompatibility and ability to provide an advantageous microenvironment for cells, the natural polymers are preferable as compared to synthetic polymers due to their biocompatibility. However, the natural polymers present low printability resolution, which can be a huge drawback for patient-specific approaches. Therefore, indirect printing can be a great alternative to fabricate 3D scaffolds using natural polymers. This strategy is based on the production of a negative mold followed by the casting of the desired polymer, typically using a drying method. The application of indirect printing approaches has proven to be a useful tool to tackle some direct printing limitations, offering both the opportunity to produce 3D scaffolds from biomaterials with mismatched processing properties and thermally unstable materials such as ceramics and composites [8]. Lee et al. [9] already demonstrated the potential of this approach for developing complex constructs in terms of micro- and macroscale. In that study, we fabricated porous poly ((lactic acid) -co-(glycolic acid)) (PLGA) scaffolds using a water-based negative mold. The indirect printed scaffolds showed good biological performance, by supporting cell growth in culture. In other study, Lee et al. [10] were able to reproduce a polycaprolactone/chitosan (PCL/chitosan) human mandibular condyle implant using a gelatin negative mold. The negative mold was produced by 3D printing, followed by the mold casting of the PCL/chitosan blend. Furthermore, the scaffolds were coated with bioactive apatite, which conferred osteoinductive properties. The in vitro biological tests performed with bone marrow stromal cells showed good cell viability, with the apatite coating further enhancing cellular spreading and proliferation. Recently, Park et al. [11] created an advanced indirect 3D printing technique using an alkali-soluble photopolymer sacrificial mold produced by projection-based microstereolithography. In that study, PCL scaffolds were fabricated by either solvent-based or thermal molding using the injection molding system (IMS). The scaffolds produced by IMS showed substantial reduction in scaffold fabrication time and higher mechanical properties.

Different natural polymers have been used in indirect printing strategies revealing good outcomes [12–14]. Liu et al. [15] combined indirect printing with freeze-drying technique to produce silk fibroin (SF) scaffolds with macro- and microstructures. The produced scaffolds presented suitable mechanical properties for cartilage tissue engineering and appropriated cell migration, attachment and proliferation. In another study, Chen et al. [16] developed SF 3D scaffolds also presenting micropores and interconnected channels using thermoplastic negative molds. The in vitro and in vivo studies (12 weeks) were performed using porcine articular chondrocytes and the results revealed extracellular matrix production and maintenance of the chondrogenic phenotype. In sum, SF has been shown to present suitable features for indirect printing approaches. Thus, we hypothesized that the above-mentioned challenges of the current available treatments could probably be overcome by means of developing patient-specific hierarchical scaffolds comprising a ceramic-based bottom layer that can improve the implant anchorage.

In this work, an indirect printing approach is proposed to produce hierarchical and multilayered patient-specific meniscus implants using SF. The desired patient specificity was achieved using a well-established reverse engineering strategy as described elsewhere [6]. The gelation methods based on the enzymatic-cross-linking reactions have also

been investigated by our group which are advantageous due to the fast-setting processing, high versatility, biocompatibility and remarkable mechanical properties [17, 18]. Therefore, an enzymatic-cross-linking step was introduced during the scaffold fabrication. To the best of our knowledge, it is the first time that indirect printing approaches combining in situ enzymatic-driven gelation method are applied to the development of hierarchical SF scaffolds. The introduction of this middle step, mediated by horseradish peroxidase (HRP) and hydrogen peroxide, aims not only to produce scaffolds with better mechanical properties and adequate shape for meniscus TE, but also to enable the production of hierarchical structures. In other words, taking advantage of the tuning capability provided by the enzymatic middle step, a bottom layer composed by SF blended with calcium phosphates, namely β-tricalcium phosphate (TCP), incorporated with zinc (Zn) and strontium (Sr), was introduced. With the addition of this bottom layer, it is envisioned to enhance the interaction of the bone–scaffold to improve its anchorage properties, whose problems have been evidenced by the conventional methods [19]. Furthermore, ionic-doped β-TCP materials have shown osteogenesis and neovascularization ability, making them suitable for the strategy herein described [20, 21]. Gruchenberg et al. [22] have already shown the difficulty in implant fixation using a silk scaffold. They reported an in vivo trial using a sheep model and, after 6 months, the constructs were not firmly fixed in the defect, which led to the appearance of a gap between the native tissue and the construct and/or its total loss. In order to produce the molds, fused deposition modeling (FDM) was used since it is the most common 3D printing method, mainly due to easy handling and cost-efficiency. The choice of the mold polymer fell in the acrylonitrile–butadiene–styrene (ABS). ABS is a cost-effective engineering polymer, easy to process and fabricate, and it has good impact resistance, excellent machinability, as well as appropriate strength and stiffness [23].

Furthermore, freeze-drying was used as drying method, whereas it was found to be the most suitable for indirect printing strategies. This method causes less shrinkage, resulting in a precise reproduction of the envisioned architecture [8]. The produced indirect printed hierarchical SF scaffolds were characterized in terms of physicochemical properties and in vitro and in vivo biological performance. The scaffolds morphology and architecture were evaluated by scanning electron microscopy (SEM) and micro-computed tomography (micro-CT), respectively, whereas the chemical structure was studied by Fourier transform infrared spectroscopy (FTIR). In vitro assays were also performed in order to assess the degradation, swelling, mechanical behavior and bioactivity. Biological performance of human meniscus cells (hMCs) and human primary osteoblasts (hOBs) seeded onto the SF scaffolds were also assessed up to 7 days of culture. In addition, in vivo assays were performed through subcutaneous implantation in mice in order to evaluate possible inflammatory response.

Materials and methods

Materials

Silkworm *Bombyx mori* cocoons were provided by the Portuguese Association of Parents and Friends of Mentally Disabled Citizens (APPACDM, Castelo Branco, Portugal). Acrylonitrile butadiene styrene (ABS) was purchased from Leapfrog (Netherlands). Human primary osteoblasts (hOBs) were purchased from Sigma-Aldrich (St. Louis, MO, USA). All reagents were purchased from Sigma-Aldrich (St. Louis, MO, USA) unless otherwise stated.

## Production of indirect printed hierarchical scaffolds

Production of ABS molds through a rapid prototyping approach

The ABS molds were designed using a commercial computer-aided design (CAD) software (Autodesk Inventor Professional 2017, Autodesk) and manufactured using a Creatr Dual Extruder 3D Printer (Leapfrog, Netherlands) (Fig. 1ai, aii). The design selected for the mold was a cube shape with 36 mm^2 of base area and 5 mm of height. Properly centered, it was also designed four cylindrical pillars with 5 mm of height and 1 mm of diameter. The molds were used to produce all the scaffolds for further characterization. In addition, by using a human meniscus model previously developed in our group through a reverse engineering approach [6], an ABS human meniscus mold was printed in order to produce an indirect printed hierarchical patient-specific meniscus implant.

Preparation of SF solution

Purified SF solution was prepared by removing the glue-like protein sericin from the cocoons in a 0.02 M boiling sodium carbonate solution for 1 h, followed by rinsing with distilled water. Then, the purified SF was dissolved in a 9.3 M lithium bromide solution for 1 h at 70 °C and dialyzed in distilled water for 48 h using a benzoylated dialysis tubing (MWCO: 2 kDa). The obtained SF aqueous solution was concentrated using 20% (w/v) poly(ethylene glycol) for at least 6 h. The final concentration of SF was determined by assessing the dry weight of the solution placed overnight at 70 °C. The SF was diluted to 16 and 8% (w/v) in distilled water and stored at 4 °C until further use.

Fig. 1 Scheme of the production of indirect printed scaffolds. **a** Different steps were required to produce indirect printed cube-shaped hierarchical scaffolds: (ai) design of the negative mold, (aii) printing of the negative mold, (aiii) mold casting of the SF and (aiv) SF blending with β-tricalcium phosphate. The same strategy was used to produce patient-specific indirect printed hierarchical scaffolds of human meniscus: (bi) model of the negative mold, (bii) patient-specific meniscus scaffold and (biii) patient-specific meniscus scaffold tightly compressed and total original shape recovery. Scale bars: 1 cm
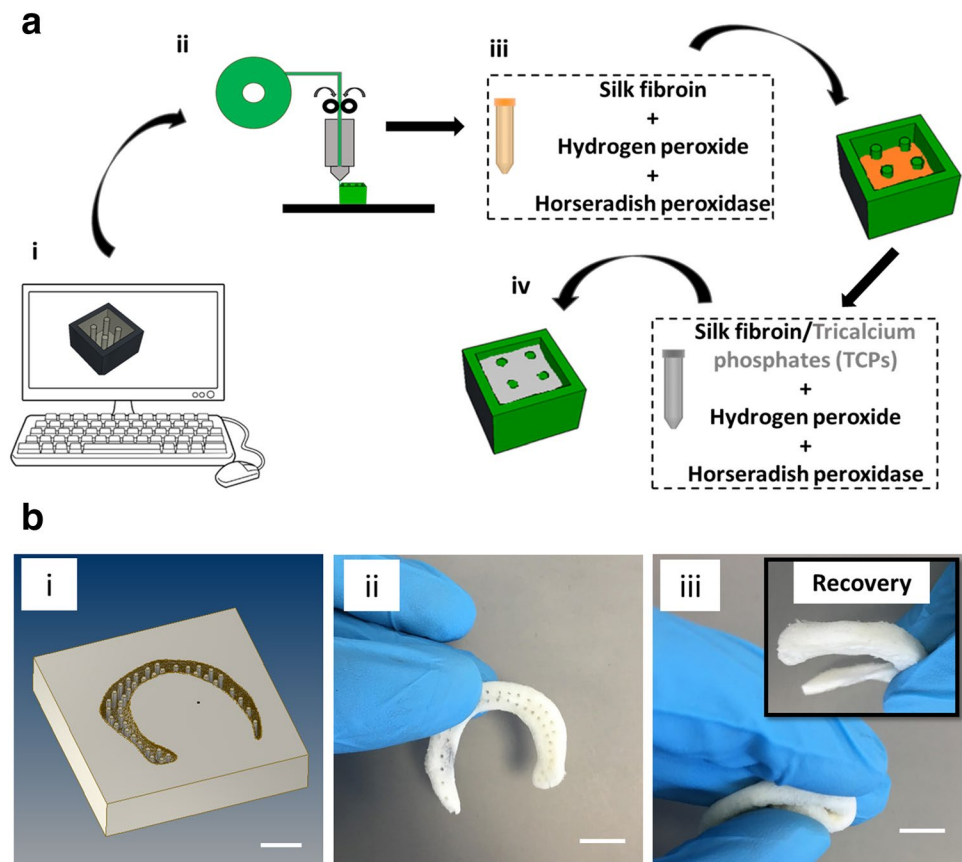
Preparation of ionic-doped β-tricalcium phosphate powders

β-Tricalcium phosphate (TCP) powders doped with 10 mol % of Sr and Zn were prepared as described elsewhere [21]. Briefly, the powders were synthesized by aqueous precipitation using adequate starting chemical precursors for calcium, phosphorous, Sr and Zn, with molar ratio of $(Ca+X)/P = 1.48$, (where X corresponds to $Sr+Zn$) and pH of ~ 7. The precipitated suspensions were kept for 4 h under constant stirring and matured for further 20 h under rest conditions, at 50 °C. The resulting precipitates were filtered, dried at 100 °C and heat-treated for 2 h at 1100 °C, followed by milling and sieving by a mesh size of 63 µm, yielding a final average particle size of ~ 1–10 µm.

Mold casting

Hierarchical indirect printed scaffolds were fabricated comprising two layers, i.e., SF layer in the upper zone and SF mixed with ionic-doped TCP in a bottom layer. For that, enzymatic-cross-linked SF hydrogels were firstly prepared by mixing SF solutions [with 8 or 16%(w/v)] with 10% (v/v)

horseradish peroxidase solution (HRP type VI, 0.84 mg mL^{-1}) and 6.5% (v/v) hydrogen peroxide solution (H_2O_2, 0.36% w/v; Panreac, Barcelona, Spain), and a total volume of 200 µL was used to fill the cube shape mold (Fig. 1aiii). The incubation was performed at 37 °C for 15 min for SF [16% (w/v)] and 25 min for SF [8% (w/v)]. For the bottom layer, using the above-mentioned enzymatic-cross-linking process, 150 µL of SF solutions [8 or 16% (w/v)] were mixed with ionic-doped TCP powder using blend ratios of 80/20 (w/w) of SF/ionic-doped TCP and added on the top of the SF layer, followed by incubation at 37 °C for 30 min (Fig. 1iv). After the gelation process, the final indirect printed scaffolds were frozen at − 80 °C and lyophilized during 3 days (CRYODOS-80; Telstar, Barcelona, Spain). The scaffolds were posteriorly immersed in a 70% (v/v) ethanol solution and easily removed from the molds. The indirect printed hierarchical scaffolds produced were abbreviated to Hi8 and Hi16 when SF solutions at 8% and 16% (w/v) were used, respectively. For further characterization, pure SF monolayer scaffolds (SF8 and SF16) and SF/TCPs monolayer scaffolds (SF8/TCP and SF16/TCP) were also prepared.

Physicochemical characterization of the indirect printed hierarchical SF scaffolds

Scanning electron microscopy (SEM)

The morphology of the Hi8 and Hi16 scaffolds was observed under an SEM (Nova NanoSEM 200; FEI, Hillsboro, OR, USA) with a coupled energy-dispersive X-ray detector (EDS). Prior to analysis under SEM, the scaffolds were coated with gold/palladium (Au/Pd) (SC502–314B) in a coater (E6700; Quorum Technologies, East Grinstead, UK). The elemental composition was performed by energy-dispersive spectroscopy (EDS; Pegasus X4M) coupled to the SEM. For EDS analysis, independent regions were selected in the SF8, SF16, SF8/TCP and SF16/TCP scaffolds.

Micro-computed tomography (micro-CT)

The micro-architecture of the scaffolds was investigated using a high-resolution micro-CT Skyscan 1072 scanner (Skyscan, Kontich, Belgium) with a pixel size of 10 μm. Standardized cone-beam reconstruction software (NRecon v1.4.3, SkyScan) was used for data sets reconstructions. Representative data set of the samples was segmented into binary images with a dynamic threshold of 22–40 (gray values). Then, the binary images obtained were used for morphometric analysis (CT Analyser, v1.5.1.5, SkyScan) and construction of three-dimensional models (ANT 3D creator, v2.4, SkyScan).

Fourier transform infrared spectroscopy (FTIR)

The structural conformation and chemical composition of the top layer and bottom layer of Hi8 and Hi16 were evaluated by FTIR spectroscopy (Perkin-Elmer 1600 series equipment, CA, USA) under an attenuated total reflectance (ATR) model (IRPrestige-21, Shimadzu, Japan). All spectra were obtained between 4600 and 800 cm^{-1} at a 4 cm^{-1} resolution with 50 scans.

In vitro degradation

The stability of the hierarchical scaffolds was assessed by enzymatic degradation assay. Protease XIV solution (1.0 U mL^{-1}) was prepared by dissolving the enzyme in distilled water. The initial weight of the scaffolds was measured, and then, the scaffolds were hydrated in PBS at 37 °C overnight, followed by immersion in 5 mL of protease solution. The enzyme solution was changed every 48 h. The samples were weight after 0.16, 0.33, 1, 7, 14, 21 and 28 days of immersion in the degradation solution at 37 °C in static conditions. The weight loss ratio was obtained using Eq. 1:

$$\text{Weight loss ratio} = \frac{(m_i - m_{d,t})}{(m_i)} \times 100\% \qquad (1)$$

where m_i is the initial weight of the sample, and $m_{d,t}$ is the weight of the degraded sample at each time point ($n = 3$ per group).

Swelling ratio

The swelling ratio of the hierarchical scaffolds was also evaluated after immersion in PBS for time periods ranging from 3 h to 28 days. All experiments were conducted at 37 °C in static conditions. At each time point, the samples were removed from PBS, the excess of surface water was absorbed using a filter paper, and the weight immediately determined. The swelling ratio was obtained using Eq. 2:

$$\text{Swelling ratio} = \frac{(m_{w,t} - m_i)}{(m_i)} \times 100\% \qquad (2)$$

where m_i is the initial weight of the sample, and $m_{w,t}$ is the wet weight of the sample at each time point ($n = 3$ per group).

Mechanical properties

The viscoelastic measurements were investigated using a TRITEC8000B dynamic mechanical analyzer (DMA; Triton Technology, UK) in the compressive mode. The indirect printed scaffolds were immersed in PBS overnight at 37 °C. The geometry of the indirect printed scaffolds was measured (with a micrometer of precision), clamped in the DMA apparatus and immersed in a PBS bath with the temperature set to 37 °C. After equilibration at 37 °C, the DMA spectra were obtained during a frequency scan between 0.1 and 10 Hz. A constant strain amplitude of 50 μm was applied in each experiment.

Uniaxial compressive tests were performed using a Universal Testing Machine (Instron 4505) with a 1 kN load cell at room temperature (RT). As previously, the scaffolds were immersed in PBS overnight at 37 °C. The cross-head speed was set at 2 mm min^{-1}, and tests were run until achieving a 60% reduction in specimen height. The elastic modulus was defined by the slope of the initial linear section of the stress–strain curve. A minimum number of 5 samples were tested per condition, with the compressive modulus values being the average of all the measurements.

In vitro characterization of the indirect printed hierarchical scaffolds

The in vitro characterization was performed only for the monolayers SF8, SF16, SF8/TCP and SF16/TCP, which was considered to be the easiest way to analyze the results obtained from these assays.

In vitro bioactivity evaluation

To evaluate the in vitro bioactivity of the scaffolds before cell cultures, the scaffolds were placed into polystyrene flasks containing ($1.5\times$) simulated body fluid (SBF) with ionic concentrations (Na$^+$ 213.0, K$^+$ 7.5, Ca^{2+} 3.75, Mg^{2+} 2.25, Cl$^-$ 223.2, HPO$_4^{2-}$ 1.5, HCO$_3^{2-}$ 6.3, SO$_4^{2-}$ 0.75 mM L^{-1}, pH ~ 7.4) nearly equivalent to the human blood plasma, as reported by Tas et al. [24]. The scaffolds were continuously shaken at a rate of 60 rpm, at 37 °C, and the liquid was refreshed every 2 days. Then, the scaffolds were allowed to dry at 37 °C for 1 day and analyzed by means of SEM/EDS analyses. All experiments were carried out in triplicate for each separated layer.

Human meniscus cells isolation and expansion

Human meniscus cells (hMCs) were isolated from meniscus tissue samples obtained from surgery procedures performed after patient's informed consent and using a protocol previously established with the Orthopedic department of Póvoa de Varzim Hospital (Póvoa de Varzim, Portugal). hMCs were isolated following an enzymatic digestion-based method (collagenase type II) from human meniscus tissue obtained from patients submitted to surgery. The extracted tissue was placed in PBS solution (pH 7.4) and washed several times with PBS containing 1% (v/v) antibiotic/antimycotic mixture until total removal of blood or other bodily contaminants. Meniscus tissue was then separated from fat and vascularized tissue, and after being washed several times, the meniscus was cut into small pieces. Tissue digestion was performed by incubation at 37 °C in a water bath for 24 h in 10–20 mL of a mixture of cell medium alpha-MEM supplemented with 10% (v/v) fetal bovine serum (FBS; Biochrom AG, Germany), 1% (v/v) antibiotic/antimycotic solution (final concentration of penicillin 100 units.mL^{-1} and streptomycin 100 mg mL^{-1}; Gibco, GB) mixture and collagenase type II (1:1). The isolated hMCs were then expanded in basal medium consisting alpha-MEM w/o nucleosides (MEM alpha medium; Life Technologies, Scotland) supplemented with 10% (v/v) FBS and 1% (v/v) antibiotic/antimycotic solution. Cells were cultured until confluence at 37 °C in an atmosphere of 5% CO$_2$ incubator, changing the culture medium every 2 days.

Human primary osteoblasts expansion

Human primary osteoblasts (hOBs) were cultured in non-coated T150 cell culture flasks using human osteoblasts growth medium (Sigma-Aldrich, St. Louis, MO, USA). Cells were cultured until confluence at 37 °C in an atmosphere of 5% CO$_2$ incubator, changing the culture medium every 2 days.

Seeding of hMCs and hOBs

The in vitro tests were performed using two different cell types. Before cell seeding, all scaffolds were sterilized overnight in ethanol and washed 3 × in PBS. Then, the samples were incubated in alpha-MEM overnight. In the following day, the scaffolds were transferred to 24-well suspension cell culture plates (Cellstar, Greiner Bio-One, Austria). Confluent hMCs (at passage 4–5) were detached with TrypLE Express (1X) (Life Technologies, Carlsbad, CA, USA) and seeded in the SF8 and SF16 scaffolds at a density of 1.5×10^5 cells/scaffold. The hOBs after confluence were also detached with TrypLE Express (1X) (Life Technologies, Carlsbad, CA, USA) and seeded SF8/TCP and SF16/TCP scaffolds at a density of 1.5×10^5 cells/scaffold. Each scaffold was kept in the CO$_2$ incubator at 37°C for 2 h, and then, 3 mL of the respective culture medium was added to each well. Samples were retrieved at different culture times (1, 3 and 7 days), and the culture medium was changed every 2 days.

Cell viability and metabolic activity

Cell viability was microscopically assessed by live/dead assay. Briefly, cell-seeded scaffolds were immersed in a calcein AM/propidium iodide (PI) solution at 1:3 ratio in culture medium for 25–30 min. The scaffolds were transferred for an incubator at 37 °C in an atmosphere of 5% CO$_2$, protected from light. Viable cells metabolize calcein AM (Invitrogen, USA 1 mg mL^{-1}) into green fluorescent calcein (Ex/Em ~ 495/515 nm), while dead cells find their DNA stained red by PI (Invitrogen, USA 1 mg mL^{-1}; Ex/Em ~ 493/636 nm). After a washing step with PBS, samples were imaged using a transmitted and reflected light microscope (Zeiss Axio Imager.Z1 m, Zeiss, Germany).

hMCs and hOBs metabolic activity was evaluated using Alamar Blue (AB). This dye yields a fluorescent signal and a colorimetric change when incubated with metabolically active cells. Cell culture medium containing 10% AB was added to the different culture wells and incubated for 4 h at 37 °C in an atmosphere of 5% CO$_2$. Then, 100 µL of solution from each well was transferred to white opaque 96-well plates, in triplicates. Fluorescence was monitored

at Ex/Em ~ 530/590 nm, using a microplate reader (Synergy HT, BioTek Instruments, USA). PBS was used to wash the AB reagent, and fresh medium was added. The metabolic activity values were calculated by normalization with the mean fluorescence value obtained for the controls (scaffolds without cells).

Cell proliferation

The quantity of double-strained DNA (dsDNA) was determined using a fluorimetric dsDNA quantification kit (Pico-Green, Molecular Probes, Invitrogen Corporation, USA). The assay was performed according to the manufacturer's instructions. This test is based on the principle that the quantity of double-strained DNA is directly proportional to cell number. After each time point, samples were washed twice with PBS solution and kept in 1 mL of ultrapure water at -80 °C until further analysis. Constructs were thawed at RT, sonicated for 1 h to induce complete membrane lysis. After sonication, the scaffold was discarded. Solution fluorescence was measured at an excitation wavelength (λ) of 485/20 nm and at an emission λ of 528/20 nm, in a microplate reader (Synergy HT, BioTek Instruments, USA). The quantification of dsDNA was calculated according to a standard curve prepared with concentrations ranging between 0 and 2 µg mL^{-1}, relating quantity of DNA and fluorescence intensity. Scaffolds without cells were used as controls.

In vivo biocompatibility assessment of the indirect printed hierarchical scaffolds

As aforementioned, the in vivo studies were assayed for the monolayers SF8, SF16, SF8/TCP and SF16/TCP, which was considered to be the easiest way to analyze the results.

Subcutaneous implantation

The maintenance and use of animals were carried out in accordance with the Ethics Committee of University of Minho and approved by the Portuguese Licensing Authority (DGV-DSSPA). Six mice Hsd:ICR (CD-1) of 5 weeks old and average weight of 25–30 g (Charles River Laboratories, Massachusetts, USA) were used in this study. Each mouse was anesthetized by intraperitoneal injection: ketamine (25 mg/Kg) and medetomidine (0.15 mL/Kg) for anesthesia; cephalexin (15 mg/kg) as antibiotic; and bupivacaine and pethidine (5–10 mg/kg) as analgesic. The mice hair was shaved at the implantation area, followed by disinfection with 70% ethanol and iodine. In each mouse, four skin incisions (1 cm length) were made in the dorsal midline, one close to the head (CH) and the other far from the head (FH). In the following, one specimen of each formulation (SF8, SF16, SF8/TCP and SF16/TCP) was implanted

subcutaneously into the respective pocket and then the skin was sutured. Four specimens of both formulations were implanted. Eight weeks post-surgery, the mice were killed by injection of overdose pentobarbital sodium followed by harvesting of the implanted materials. The explants were fixed with 10% (v/v) formalin solution (Sigma-Aldrich, Germany) for 24 h at RT and then transferred to histological cassettes. Sections were prepared by cutting the specimen into 20-µm-thick sections using a microtome (Spencer 820, American Optical Company, NY, USA). The obtained sections were stained with hematoxylin and eosin (H&E) and Masson's trichrome (MT).

Statistical analysis

All the numerical results are presented as mean $\pm$ standard deviation (SD). Statistical analysis was performed using the GraphPad Prism 5.0 (GraphPad Software, La Jolla, CA, USA). First, a Shapiro–Wilk test was used to ascertain regarding data normality. For all the biological quantification assays, the differences between the experimental results were analyzed using a Kruskal–Wallis test followed by Dunn's multiple comparison test. Three independent experiments were performed for cell studies (metabolic activity and cell proliferation), and three samples were analyzed per group in each culturing time. The significance level was set to *$p < 0.05$, **$p < 0.01$, ***$p < 0.001$.

Results

As aforementioned, a meniscus model previously developed by our group [6] was herein used to produce a negative mold (Fig. 1bi). As it can be seen in Fig. 1bii, biii, the presented indirect printing strategy enabled the fabrication of hierarchical patient-specific implants with the meniscus native shape. Cube-shaped molds with 36 mm^2 of base and 5 mm of height were designed with four properly centered cylinders with 1 mm of diameter to produce smaller scaffolds for characterization (Fig. 2a, b). The mold design was chosen, not only to simplify the subsequent characterization, but also to show the tuning capability of our approach in terms of mold architecture. Two different SF (8 and 16% w/v) solutions were used to produce the indirect printed scaffolds in order to evaluate the influence of the polymer concentration (Fig. 2c–f). From Fig. 2d–f, it is possible to observe the hierarchical indirect printed scaffolds, as well as the two well-defined layers: the top layer composed only by SF and the bottom layer composed by 80/20 (w/w) ratio of SF/TCP (i.e., Hi8 and Hi16). The hierarchical structure was obtained after optimized steps (data not shown) and resulted from the use

Fig. 2 Macroscopic images of the indirect printed cube-shaped scaffolds. **a**, **b** Macroscopic images of the negative molds, **c**, **d** Hi8, and **e**, **f** Hi16. Scale bars: 2 mm (**a**–**c**, **e**); and 1 mm (**d**, **f**)
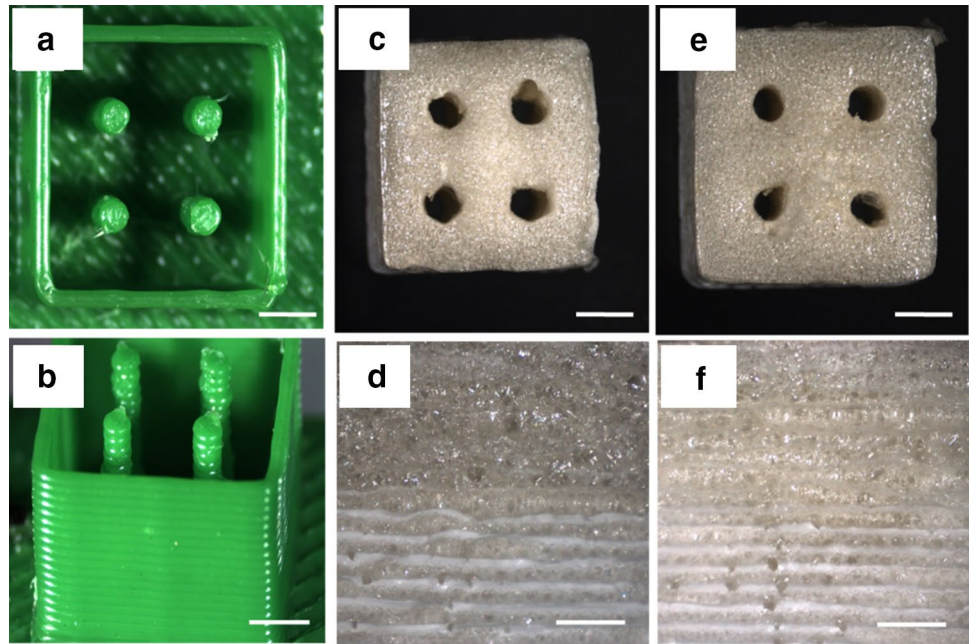
of the enzymatic-cross-linking middle step. In short, after the cross-linking reaction of the SF8/TCP and SF16/TCP solutions that occurred for 25 min and 15 min, respectively, it was possible to add a pure SF solution on the top to create a hierarchical structure. In fact, the cross-linking reaction time was optimized in order to obtain a distinct separation zone, as well as a good integration of both layers.

Morphology and microstructure

The pore morphology and the quantitative and qualitative analysis of porosity were assessed by means of SEM and micro-CT analyses, respectively (Fig. 3). From SEM images (Fig. 3a), it is possible to observe the pore morphology of both scaffold formulations (Hi8 and Hi16) and the presence of TCP in the bottom layer. The porosity observed was induced by the freeze-drying technique used in the production of scaffolds, and it is characterized by pores with size ranging from 60 µm to 110 µm. Comparing both layers, larger pores were observed in the bottom layers of the hierarchical scaffolds possibly due to the higher integrity conferred by the ceramic powders. A 3D reconstruction of the Hi8 and Hi16 scaffolds was also performed by micro-CT (Fig. 3b). From the 3D image, it can be observed that the scaffolds present a high degree of porosity. It can also be clearly distinguished the difference between the ceramic bottom layer and the pure silk top layer. No significant differences in terms of mean porosity, pore size and trabecular thickness were observed comparing both formulations. The morphometric analysis confirmed the similarity of both formulations in terms of mean porosity, mean pore size and mean trabecular thickness (Table 1). The mean porosity of

Hi8 and Hi16 was $74.1 \pm 1.4\%$ and $72.9 \pm 3.1\%$, respectively. The Hi8 scaffold presented a mean pore size and trabecular thickness of 119.7 ± 11.5 µm and 32.2 ± 3.2 µm, respectively, whereas the Hi16 scaffold revealed slightly higher values of mean pore size (126.9 ± 18.9 µm) and trabecular thickness (40.7 ± 0.5 µm). Comparing the different layers of the scaffolds, higher values of mean pore size and trabecular thickness where found in the bottom layer. The higher values of trabecular thickness can be explained by the presence of TCP. In addition, the presence of TCP enhances the structural integrity leading to more homogeneous pores in the bottom layer, which can be an explanation for the slightly high values of pore size. However, no significant differences were observed in terms of pore geometry and morphology between the Hi8 and Hi16 scaffolds.

Chemical structure

The SF conformation and the presence of the ceramics were evaluated by ATR-FTIR analysis (Fig. 4a). Regarding silk conformation, the predominance of β-sheet conformation was confirmed by the presence of the characteristic peaks at 1623 cm^{-1} and 1526 cm^{-1}. Additionally, the bottom layers spectra of the Hi8 and Hi16 scaffolds showed the appearance of a main peak around 1030 cm^{-1}. This new peak is related to the characteristic vibrational modes of the PO_4 group in the ionic-doped TCP [21]. In a another work, Yan et al. [25] developed silk scaffolds containing calcium phosphate powders. After ATR-FTIR analysis, a similar spectrum was obtained revealing the presence of the ceramic powders and the predominance of β-sheet conformation.
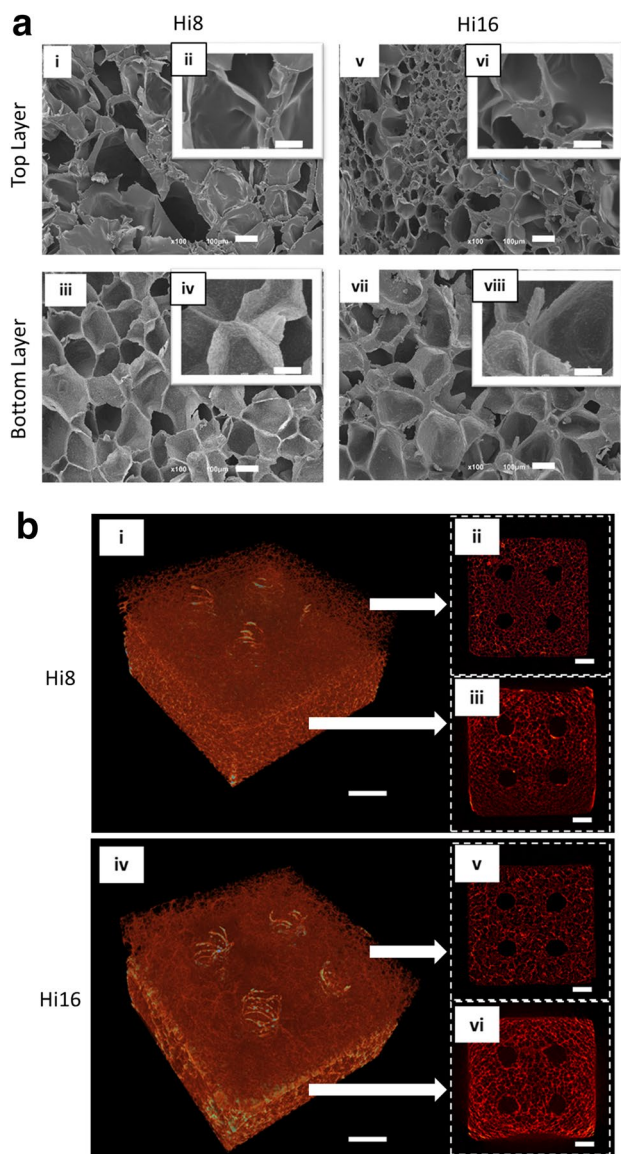
Table 1 Microstructure of the indirect printed hierarchical scaffolds analyzed by micro-CT

	Mean porosity (%)	Mean pore size (μm)	Mean trabecular thickness (μm)
Hi8			
Top layer	75.9 ± 1.3	113.3 ± 22.9	30.7 ± 2.9
Bottom layer	73.8 ± 1.5	125.0 ± 24.4	50.7 ± 0.5
Total scaffold	74.1 ± 1.4	119.7 ± 11.5	32.2 ± 3.2
Hi16			
Top layer	72.2 ± 1.8	117.0 ± 18.7	37.3 ± 0.5
Bottom layer	75.9 ± 1.5	137.5 ± 22.6	55.7 ± 0.9
Total scaffold	72.9 ± 3.1	126.9 ± 18.9	40.7 ± 0.5

After 21 days, the Hi8 was completely degraded whereas the Hi16 scaffold presented $64.4 \pm 8.4\%$ of degradation. However, at the end of the test (28 days), the Hi16 scaffold was completely degraded. The formulation with lower concentration of silk presented, as expected, higher degradation ratios and a faster degradation. Regarding the water uptake capacity of these scaffolds, higher values of swelling were presented by the Hi8 scaffolds in the first 5 days of immersion in PBS (Fig. 4c). This difference was only noted up to 5 days, when the scaffolds reached a similar pattern of swelling. Nevertheless, after 28 days Hi8 and Hi16 scaffolds revealed values of swelling of $148.3 \pm 23.7\%$ and $150.5 \pm 21.1\%$, respectively. Despite the high swelling capacity demonstrated by both formulations, it is important to emphasize that they maintained their shape after 28 days in PBS solution.

Mechanical properties

The mechanical properties of both formulations were assessed by DMA and by performing a uniaxial compression test (INSTRON). The viscoelastic properties were analyzed by DMA in a range of frequencies from 0.1 to 10 Hz (Fig. 4d, e). The formulations with higher silk concentration revealed higher values of storage modulus (E') (Fig. 4d) and lower values of damping factor (tan δ) (Fig. 4e). The storage modulus of Hi8 and Hi16 increased from 1.03 ± 0.08 to 1.56 ± 0.13 MPa and from 2.17 ± 0.25 to 3.19 ± 0.38 MPa, respectively. Furthermore, the damping factor values were very similar comparing Hi8 and Hi16 scaffolds, with slightly higher values in the Hi8 formulation. Thus, the scaffold with lower concentration of silk (Hi8) has a slightly higher propensity to disperse energy under a compressive force.

Figure 4f shows the representative stress–strain plot of the developed hierarchical scaffolds. The values of compressive modulus were higher for Hi16 (0.66 ± 0.05 MPa) as compared with Hi8 (0.27 ± 0.08 MPa). In short, the results obtained by the uniaxial compressive test corroborate the

Fig. 3 SEM images and 3D reconstruction of the indirect printed hierarchical scaffolds. **a** SEM images of Hi8 and Hi16 scaffolds at different magnifications from the top layer (ai, aii and av, avi, respectively) and bottom layer (aiii, aiv and avii, aviii, respectively). **b** 3D reconstruction by micro-CT of the Hi8 and Hi16 (bi and biv, respectively), 2-D images from the top layer (bii and bv, respectively), and bottom layer (biii and bvi, respectively). Scale bars: 500 μm (ai, iii, v and vii), 50 μm (aii, vi, iv and viii) and 1 mm (bi–vi)

Degradation and swelling properties

The degradation profile of the Hi8 and Hi16 scaffolds was evaluated using protease XIV (Fig. 4b). After 1 day, only $4.3 \pm 2.6\%$ and $2.7 \pm 2.8\%$ of degradation was observed for the Hi8 and Hi16 scaffolds, respectively. Nevertheless, the degradation percentage increased significantly in the following 7 days with the Hi8 and Hi16 scaffolds presenting $48.8 \pm 9.9\%$ and $75.1 \pm 16.2\%$ of degradation, respectively.
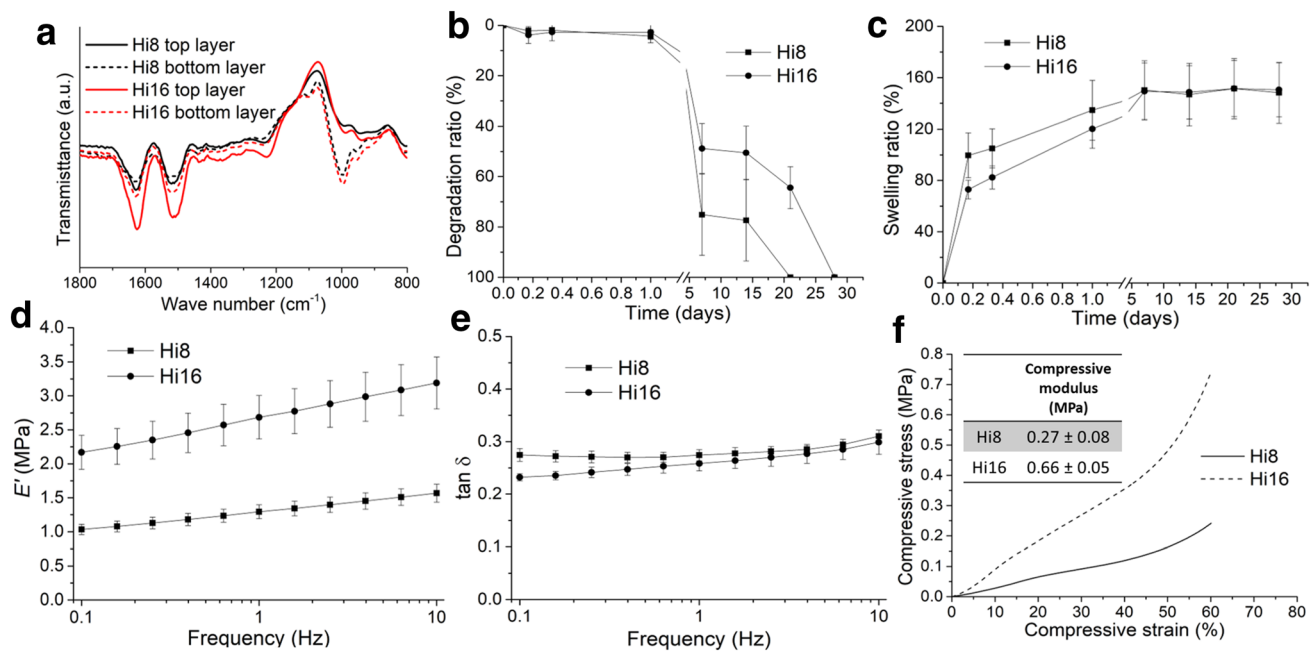
Fig. 4 Chemical analysis, degradation and swelling behavior, and mechanical performance of the indirect printed hierarchical scaffolds. **a** ATR-FTIR spectra of the Hi8 and Hi16 top and bottom layers. **b, c** Degradation and swelling profiles of the Hi8 and Hi16, obtained in protease XIV and PBS solutions, respectively. **d, e** Storage modulus (E') and damping properties of the Hi8 and Hi16 obtained by DMA. **f** Stress–strain plot of the Hi8 and Hi16 and respective compressive modulus

previous data obtained by DMA analysis, showing that the polymer concentration has a critical role in the mechanical behavior.

The mechanical properties of SF8, SF16, SF8/TCP and SF16/TCP scaffolds were also assessed (Supplementary Figs. 1–3 and Supplementary Table 1). It was observed that the presence of TCP provided an increase in terms of stiffness and a decrease of their damping properties.

In vitro bioactivity of the indirect printed scaffolds

The bioactivity of the scaffolds was evaluated on the top and bottom layers of Hi8 and Hi16 by soaking the scaffold in a SBF solution (Fig. 5). Results showed that the Hi8 and Hi16 bottom layers (Fig. 5b and e, respectively) appeared partially covered with cauliflower-like of apatite crystals, while no apatite crystals were induced on the top layers of Hi8 and Hi16 (Fig. 5a and c, respectively), after 7 days of soaking This apatite crystal morphologies are comparable to that of hydroxyapatite (HAp) also confirmed by the quantified Ca/P ratio obtained from EDS elemental analysis (Fig. 5c, f).

Attachment, viability and proliferation of hMCs and hOBs on the indirect printed scaffolds

As mentioned before, scaffolds composed only by pure SF (SF8 and SF16) and SF blended with TCP (SF8/TCP and SF16/TCP) were produced in order to assess the biological performance of both layers of the hierarchical scaffolds. The SF8 and SF16 were seeded with hMCs, whereas the SF8/TCP and SF16/TCP were seeded with hOBs. From the live/dead staining, it was observed that the hMCs and hOBs were viable over the 7 days of culture (Fig. 6a). From day 1 to day 7, an increase in fluorescence was detected, indicating that cells adhered to the indirect printed scaffolds and proliferated. The cells were well dispersed in the scaffolds surface and presented the typical spreading morphology after 7 days of culturing. The cells metabolic activity and proliferation were quantified by Alamar Blue assay and DNA content analysis, respectively. The results of metabolic activity were normalized with the DNA content (Fig. 6b). In the scaffolds seeded with hMCs (Fig. 6bi), a significant increase from day 1 to day 7 (***$p < 0.001$) was observed for both formulations. However, no statistically significant differences were observed when comparing the SF8 with SF16 scaffolds. For both the SF8/TCP and SF16/TCP scaffolds (Fig. 6bii), the in vitro biological assays revealed a significant increase from day 1 to day 3 (**$p < 0.001$) and from day 1 to day 7 (***$p < 0.001$). As for the pure silk scaffolds, no statistically significant differences were observed when comparing the scaffolds with different SF concentrations. These results could be explained by the lack of significant differences in terms of pore geometry and morphology between the Hi8 and Hi16, as previously shown in the SEM and micro-CT
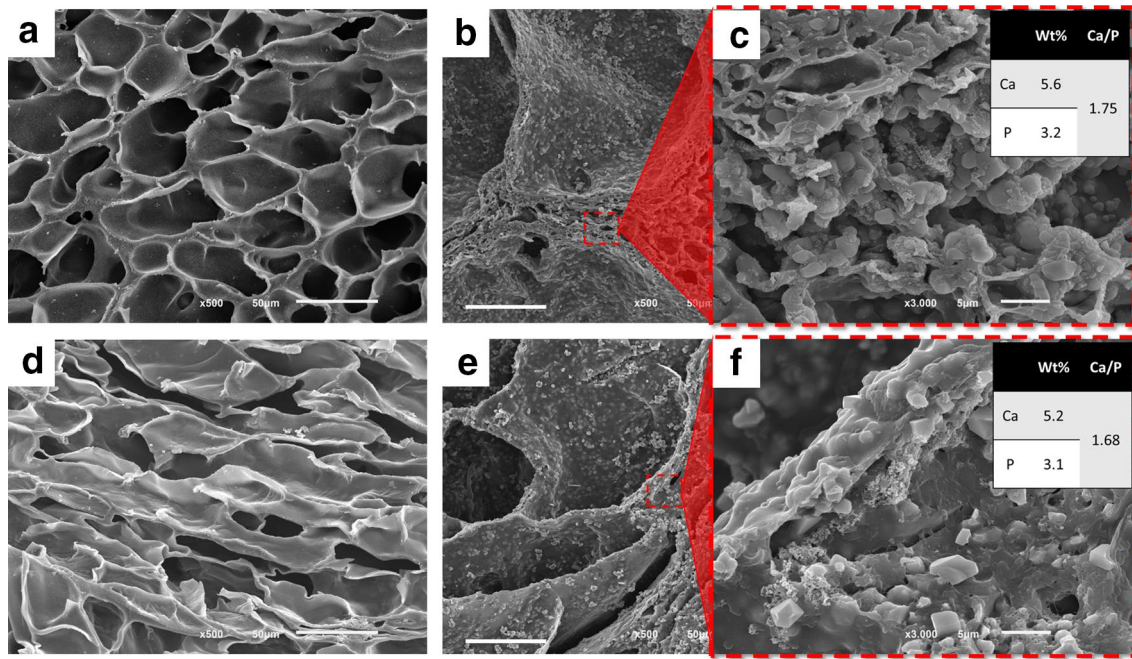
Fig. 5 SEM micrographs of Hi8 top (**a**) and bottom (**b**) layers, and Hi16 top (**d**), and bottom (**e**) layers after 7 days of mineralization, and respective Ca and P wt% obtained from EDS analysis, after mineralization. Scale bars: 50 μm (**a**, **b**, **d**, **e**); 5 μm (**c**, **f**)
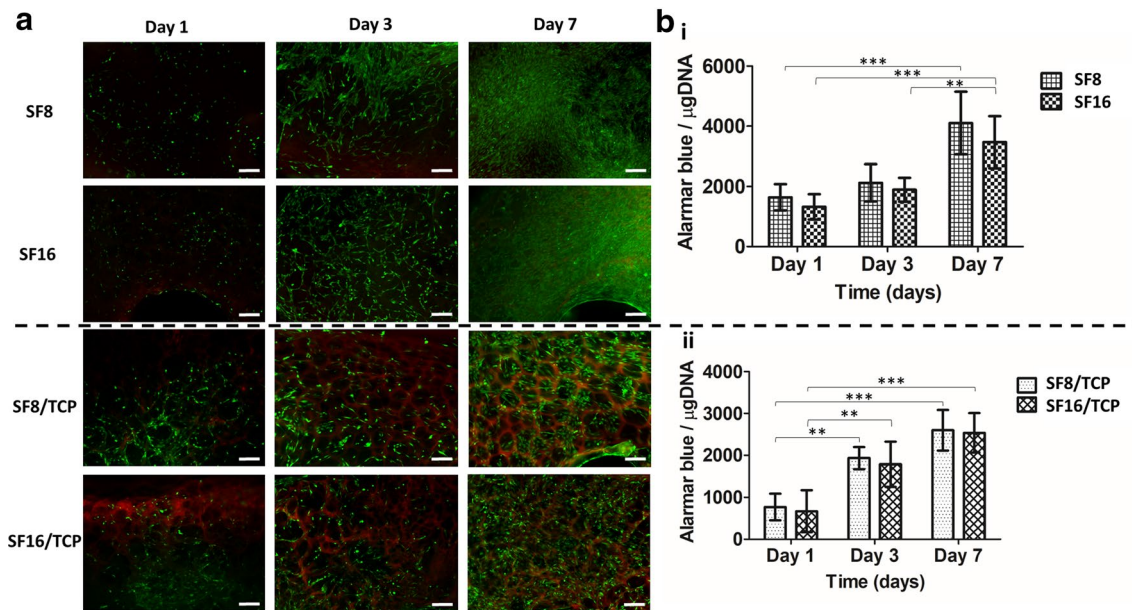

Fig. 6 In vitro biological performance of the different layers of the indirect printed hierarchical scaffolds. **a** Live/dead staining of the SF8, SF16, SF8/TCP and SF16/TCP after 1, 3 and 7 days of culturing. **b** Metabolic activity by Alamar Blue assay normalized with DNA content. Results were obtained after 1, 3 and 7 days of culturing for the SF8 and SF16 (bi) and SF8/TCP and SF16/TCP (bii). Statistically significant differences were represented by *($p < 0.5$), **($p < 0.01$) and ***($p < 0.001$). Scale bars: 200 μm
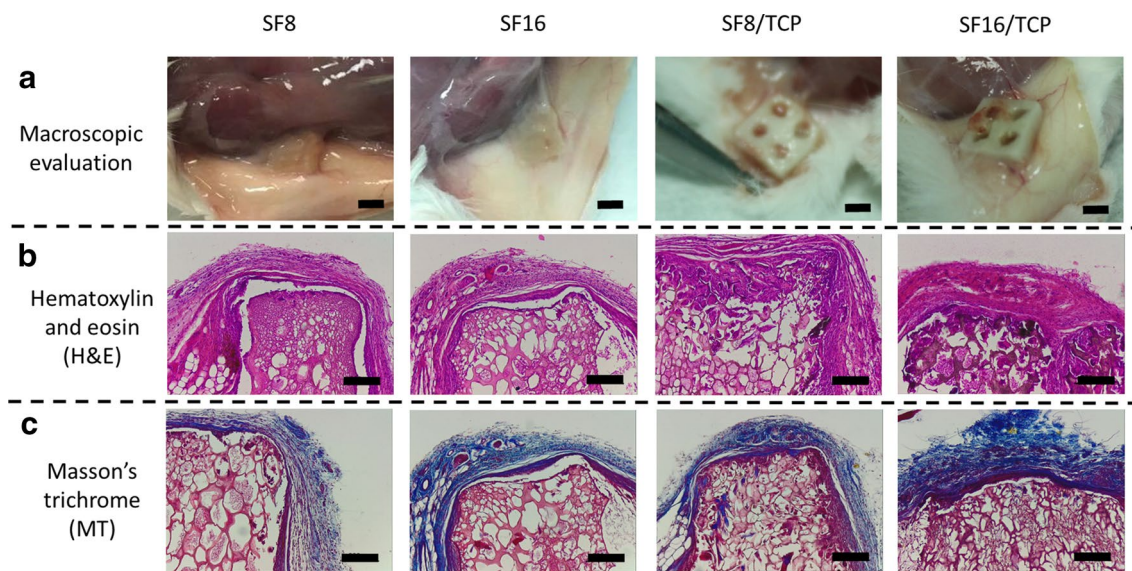
Fig. 7 Subcutaneous implantation of the different layers of the indirect printed hierarchical scaffolds in CD-1 mice for 8 weeks. **a** Macroscopic images of the explants after 8 weeks of implantation. **b** H&E staining and **c** MT staining of the explants. Scale bars: 4 mm (**a**) and 200 μm (**b**, **c**)

data. In short, the variation of the silk concentration does not have an effective impact in the scaffold's biological performance.

Subcutaneous implantation of the indirect printed scaffolds

The in vivo biocompatibility of the indirect printed scaffolds was assessed by subcutaneous implantation in CD-1 mice (Fig. 7). The macroscopic images of the explants retrieved after 8 weeks of implantation showed a good integration of the scaffolds with the host subcutaneous tissue. Nevertheless, a slightly better integration was observed in the SF8 and SF16. In addition, the scaffolds were capable of maintaining their shape and integrity over the implantation period. No signs of infection or acute inflammation were observed, with the scaffolds presenting good biocompatibility with the surrounding connective tissue. The MT staining images revealed the formation of collagenous surrounding tissue (blue fibers). Herein, no significant differences were found when comparing all formulations.

Discussion

Meniscus, as mentioned before, has a very important biomechanical function in human knee. Meniscus-limited healing capacity triggered the interest in finding new TE strategies for treating irreparable meniscus injuries. Total/partial meniscectomy has been the gold standard treatment; however, its contribution for significant arthritic changes

in the knee and non-satisfactory long-term outcomes has increased the use of conservative approaches [2, 26]. Nowadays, non-operative approaches and physical therapy programs have been used rather than meniscectomy in some traumatic and degenerative meniscal lesions. The similarity in terms of clinical outcomes between meniscectomy and the conservative strategies has been changing the paradigm, and the concept of meniscus preservation has been gaining interest among the medical community. However, the conservative strategies cannot be considered a good alternative to the current available treatments. Depending on the lesions, occasionally, conservative treatments cannot be applied. Therefore, new strategies must be developed, especially TE-based approaches, in order to achieve the desired meniscus regeneration and biofunctionality.

Different strategies have been investigated, and there are already some commercial available solutions (e.g., Actifit®, CMI® and NUsurface®), but many issues still remain to be solved, namely related with mechanical properties, degradation behavior, biocompatibility, patient specificity and anchorage [27]. In the last few years, the use of SF has extended from the textile to the TE field, due to its well-known biocompatibility, mechanical strength and degradation behavior. In this study, it is proposed the development of hierarchical patient-specific SF scaffolds for meniscus regeneration, using an indirect printing strategy to overcome conventional processing limitations, and their characterization by in vitro and in vivo studies.

The macroscopic characterization of the indirect printed scaffolds (Hi8 and Hi16) (Fig. 2c–f) revealed the reproducibility of this method, from which hierarchical scaffolds were

obtained with the proposed shape. The four similar vertical holes created by the proposed mold aimed to improve the interconnectivity and tissue ingrowth inside the scaffold. Previous works developed indirect printed scaffolds with higher porosity and interconnectivity [12, 13, 15, 16, 28]; however, it is well known that the increase in porosity leads to a decrease in the mechanical performance [29]. In this sense, it is essential to have a good balance between the porosity and the mechanical properties in order to ensure the mechanical functionality and chondroprotective effect of the scaffold. In addition to the macro-pores, micropores were formed by the freeze-drying technique (Fig. 3). Freeze-drying has been widely used for the production of porous scaffolds in the TE field [30]. This method is based on rapid cooling and subsequent solvent removal by sublimation under vacuum. Different freezing temperatures and successive freeze–thaw cycles were shown to have an impact in the scaffolds pore size and morphology [31]. The microporosity affects directly the cell behavior acting as cue for cell attachment, proliferation and production of extracellular matrix [32]. In this work, the scaffolds were frozen at $-80\,°C$ overnight and directly freeze-dried. The mean porosity values obtained were around 72.9–74.1%, whereas the mean pore size had around 119.7–126.9 µm (Table 1). In this sense, we believe that an adequate porosity and pore sizes were achieved, in combination with the macro-porosity induced by the mold design, that are suitable for a meniscus TE approach, providing a good balance between the ability for cell invasion and the mechanical performance of the scaffold. Nevertheless, it is important to preserve the idea that is possible to tune the scaffolds' macro-porosity by changing the mold design. This tuning ability can only be obtained by using a 3D printing technology. In this case, an indirect printing approach can be a faster and easier alternative when compared to direct printing. In what concerns direct printing strategies, the printing fidelity is highly dependent on the ink properties. Among these properties, the gelation time can be a huge limitation in terms of time of printing, fidelity and size of the scaffold [28, 33]. In this sense, we selected to use an indirect printing approach that allows producing patient-specific hierarchical scaffolds by printing different supporting structures.

The silk conformation and the presence of TCP in the bottom layer was assessed by ATR-FTIR (Fig. 4a). Comparing with previous studies [21, 25], the scaffolds maintained the chemical structure with predominance of the β-sheet conformation. The predominance of this type of conformation is very important in this strategy, since a previous study confirmed lower degradation ratios and higher mechanical performance in the presence of β-sheet conformation [25]. Moreover, the presence of TCP was also confirmed.

The degradation behavior of the scaffolds has a critical role in tissue engineering approaches [34]. It is important to tune the scaffolds degradation ratio in order to have a good balance between new tissues' formation and implant degradation. The possibility to tune the degradation behavior of SF scaffolds has already been shown and well investigated [35–37]. In this study, the capability for tuning degradation was demonstrated by changing the polymer concentration. The results revealed that scaffolds with higher silk concentration presented lower degradability (Fig. 4b). In a previous in vivo work, Wang et al. [38] showed that scaffolds prepared from a 10% w/v SF solution maintained their structural integrity for at least 8 weeks, while those prepared from a 6% w/v solution did not. In addition, this degradation behavior was also observed in vitro when enzymatic digestion of porous silk scaffolds was performed [39]. In this work, the developed scaffolds completely degraded upon contact to protease for 21 days. Compared with previous works [40, 41], the indirect printed scaffolds presented similar degradation profile, as well as an indirect proportionality between the silk concentration and the degradation ratio. Since the Hi16 scaffolds revealed a slower degradation ratio, they can be a better alternative for future applications in meniscus TE. The mechanical properties of the scaffolds play a major role in the total restoration of the meniscus function in the knee joint. The stabilization of the knee joint through absorption and distribution of the stress loads, as well as the prevention of early degenerative joint diseases, is directly related to the implant mechanical performance [42]. In addition, a recent study demonstrated that cartilage contact pressures and implant displacement are sensitive to the implant material stiffness [43]. The values of storage modulus (E') obtained at 1 Hz (frequency associated to normal ambulation [44]) under dynamic conditions were 1.29 ± 0.10 MPa and 1.48 ± 0.08 MPa for Hi8 and Hi16 scaffolds, respectively (Fig. 4e). Under the same conditions, two distinct works performed by Pereira et al. [45] and Bursac et al. [46] revealed similar values using human meniscus samples. In both works, E' values ranged from 0.4 to 1.7 MPa. Furthermore, under static conditions, the indirect printed scaffolds presented similar values of compressive modulus comparing with the native tissue. The results obtained from the uniaxial compression test (Fig. 4f) revealed a compressive modulus of 0.27 ± 0.08 MPa for Hi8 scaffold and 0.66 ± 0.05 MPa for Hi16 scaffold. Chia et al. [47] performed an unconfined compression test at the physiological strain rate in human frozen meniscus. The axial and radial compressive modulus measured at a physiological loading rate at 12% strain were 0.718 MPa and 0.605 MPa, respectively, suggesting again that the mechanical performance of the indirect printed scaffolds is suitable for

meniscus TE. The indirect printed scaffolds revealed not only similar mechanical behavior comparing with the native tissue but also mechanical properties comparable to other silk scaffolds produced using conventional techniques such as salt leaching, freeze-drying and gas foaming [22, 48, 49]. In a similar indirect printing approach using SF, Liu et al. [15] reported higher values of compressive modulus in scaffolds with lower concentration of silk. This might be due to the conditions used in the test, since the authors used dry scaffolds instead of wet scaffolds. However, this study also revealed a similar correlation in terms of silk concentration and mechanical performance, where the compressive modulus was found to increase with increasing SF concentrations. Besides that, the presence of TCP in the bottom layer helped to increase the stiffness of the scaffolds. This was confirmed by the mechanical tests performed in SF8, SF16, SF8/TCP and SF16/TCP scaffolds (Supplementary Figs. 1–3 and Supplementary Table 1), as well as in another study performed by our group [25]. Another important mechanical property, especially in meniscus TE applications, is the damping effect, which reduces the internal forces in the knee [50]. The produced indirect printed scaffolds showed damping factors at 1 Hz of 0.27 ± 0.01 and 0.25 ± 0.01 for Hi8 and Hi16 scaffolds, respectively. Comparing with the native tissue, these values were slightly higher. Pereira et al. [45] reported values of damping factor ranging from 0.12 to 0.18. According to the previous results and, since the indirect printed scaffolds presented higher stiffness than the native tissue, it was already expected that the indirect printed scaffolds revealed less propensity to disperse energy. Nevertheless, the mechanical performance of the indirect printed scaffolds proved to be suitable for meniscus TE presenting an adequate stiffness and viscoelastic properties.

The in vitro mineralization ability of the Hi scaffolds was investigated after soaking the scaffolds in SBF solution for 7 days (Fig. 5). Results showed the formation of apatite crystals onto the surface of Hi8 and Hi16 bottom layers (Fig. 5b, c and e, f, respectively). This result was expected due to the presence of TCP powders, as well as from the Zn and Sr presence. It is well known that these trace elements are able to improve the apatite layer deposition and mineral growth [51].

The biological performance of the scaffolds is critical for any TE application, which should allow cells to adhere and proliferate. In a preliminary cell culture assay, we decide to use pure silk scaffolds (SF8 and SF16) and scaffolds blended with TCP (SF8/TCP and SF16/TCP) seeded with different cells types. The SF8 and SF16 scaffolds were seeded with hMCs, whereas the SF8/TCP and SG16/TCP were seeded with hOBs. The aim was to mimic the physiological conditions, where meniscus cells will be in contact with the pure silk layer, whereas the osteoblasts will be in contact with the

bottom layer containing TCP. Both formulations presented good biocompatibility, showing cell adhesion and proliferation up to 7 days of culture (Fig. 6). SF has been widely exploited for TE applications [52], especially for the production of silk-based scaffolds for musculoskeletal regeneration [53]. Mandal et al. [48] developed a three-layered SF meniscal material system to mimic the meniscus architecture. In this work, human chondrocytes and fibroblasts were seeded in the SF scaffold. The cell culture results showed that the construct was a suitable template for meniscus-like tissue growth. On the other hand, it is well established that the presence of ceramics plays a major role in bone TE applications [54]. As mentioned before and based on the literature, we envisioned that the presence of TCP in the bottom layer of the indirect printed scaffolds would be a huge factor to enhance the scaffold anchorage. Using similar ceramic powders, Pina et al. [21] showed that the presence of ionic-doped TCP in silk scaffolds led to a higher osteogenic potential. These results are in line with other studies, where the presence of ceramics induced higher alkaline phosphatase activity comparing with pure silk scaffolds [25, 55]. Supported by the literature and by our results, it is expected a better interaction in the bone–scaffold interface that will possibly lead to a superior scaffold anchorage. However, further in vivo assays should be performed to confirm this hypothesis.

The biocompatibility between the indirect printed scaffolds and in vivo tissues was analyzed by subcutaneous implantation (Fig. 7). Like in the in vitro assays, only the individual SF8, SF16, SF8/TCP and SF16/TCP scaffolds were implanted. Due to the good mechanical behavior of the indirect printed scaffolds, the integrity and shape was maintained after 8 weeks of implantation. This result is in agreement with the in vitro mechanical analysis. Furthermore, the scaffolds were able to support tissue presenting good biocompatibility and a minimal inflammatory response. Similar results were found using SF-based scaffolds after 4 [56] and 12 [57] weeks of implantation. Herein, indirect printed SF scaffolds were shown to present a good in vivo biocompatibility. The good biological performance of SF-based scaffolds can be affected by the type of processing used, which is directly related to the physical and chemical properties of SF [58].

Overall, the developed scaffolds presented promising properties to be used in cartilage/fibrocartilage tissue engineering applications. The developed system showed that is possible to use different concentrations of SF to produce indirect printed hierarchical patient-specific scaffolds. Comparing both formulations, the Hi16 scaffolds presented superior mechanical properties, lower degradation ratio and similar biological performance, making it a better candidate for meniscus tissue engineering as compared to the Hi8 scaffolds.

Conclusions

In this study, novel indirect printed hierarchical scaffolds composed by a SF top layer and a SF/TCP bottom layer were developed. The use of an indirect printing approach allowed the production of scaffolds with tunable porosity and shape, as well as patient specificity. The adequate morphology and porosity, together with superior mechanical properties and suitable integrity, make these scaffolds promising candidates for meniscus regeneration. The in vitro biological assays demonstrated that the top layer and the bottom layer of the scaffolds supported the viability and proliferation of human meniscus cells and human primary osteoblasts, respectively, up to 7 days. Moreover, these scaffolds induced a very weak inflammatory response when subcutaneously implanted in mice. However, a complementary in vivo study, for example in a rabbit meniscus model, would be necessary to fully validate these indirect printing hierarchical scaffolds and confirm the hypothesis envisioned by the authors that the presence of TCP in the bottom layer of the scaffolds would enhance the anchorage properties, by improving the interaction bone-implant. Nevertheless, the in vitro and in vivo results are encouraging and confirmed the potential of the developed indirect printed hierarchical scaffolds for meniscus tissue engineering applications.

Compliance with ethical standards

Conflict of interest All the authors declare that they have no conflict of interest.

Ethical approval This article does not contain any studies with human or animal subjects performed by any of the author.

References

1. Khetia EA, McKeon BP (2007) Meniscal allografts: biomechanics and techniques. Sports Med Arthrosc Rev 15(3):114–120. https://doi.org/10.1097/JSA.0b013e3180dca217
2. Mordecai SC, Al-Hadithy N, Ware HE, Gupte CM (2014) Treatment of meniscal tears: an evidence based approach. World J Orthop 5(3):233–241. https://doi.org/10.5312/wjo.v5.i3.233
3. Abrams GD, Frank RM, Gupta AK, Harris JD, McCormick FM, Cole BJ (2013) Trends in meniscus repair and meniscectomy in the United States, 2005–2011. Am J Sports Med 41(10):2333–2339. https://doi.org/10.1177/0363546513495641
4. Costa JB, Oliveira JM, Reis RL (2017) Biomaterials in meniscus tissue engineering. In: Oliveira JM, Reis RL (eds) Regenerative strategies for the treatment of knee joint disabilities. Springer International Publishing, Cham, pp 249–270. https://doi.org/10.1007/978-3-319-44785-8_13
5. Costa JB, Pereira H, Espregueira-Mendes J, Khang G, Oliveira JM, Reis RL (2017) Tissue engineering in orthopaedic sports medicine: current concepts. J ISAKOS Joint Disord Orthop Sports Med 2(2):60. https://doi.org/10.1136/jisakos-2016-000080
6. Cengiz IF, Pitikakis M, Cesario L, Parascandolo P, Vosilla L, Viano G, Oliveira JM, Reis RL (2016) Building the basis for patient-specific meniscal scaffolds: from human knee MRI to fabrication of 3D printed scaffolds. Bioprinting 1–2:1–10. https://doi.org/10.1016/j.bprint.2016.05.001
7. Haglin JM, Eltorai AE, Gil JA, Marcaccio SE, Botero-Hincapie J, Daniels AH (2016) Patient-specific orthopaedic implants. Orthop Surg 8(4):417–424. https://doi.org/10.1111/os.12282
8. Houben A, Van Hoorick J, Van Erps J, Thienpont H, Van Vlierberghe S, Dubruel P (2017) Indirect rapid prototyping: opening up unprecedented opportunities in scaffold design and applications. Ann Biomed Eng 45(1):58–83. https://doi.org/10.1007/s10439-016-1610-x
9. Lee M, Dunn JCY, Wu BM (2005) Scaffold fabrication by indirect three-dimensional printing. Biomaterials 26(20):4281–4289. https://doi.org/10.1016/j.biomaterials.2004.10.040
10. Lee JY, Choi B, Wu B, Lee M (2013) Customized biomimetic scaffolds created by indirect three-dimensional printing for tissue engineering. Biofabrication 5(4):045003. https://doi.org/10.1088/1758-5082/5/4/045003
11. Park JH, Jung JW, Kang HW, Cho DW (2014) Indirect three-dimensional printing of synthetic polymer scaffold based on thermal molding process. Biofabrication 6(2):025003. https://doi.org/10.1088/1758-5082/6/2/025003
12. Wai-Yee Y, Chee-Kai C, Kah-Fai L, Margam C, Mun-Wai L (2006) Indirect fabrication of collagen scaffold based on inkjet printing technique. Rapid Prototyp J 12(4):229–237. https://doi.org/10.1108/13552540610682741
13. Liu CZ, Xia ZD, Han ZW, Hulley PA, Triffitt JT, Czernuszka JT (2008) Novel 3D collagen scaffolds fabricated by indirect printing technique for tissue engineering. J Biomed Mater Res Part B Appl Biomater 85(2):519–528. https://doi.org/10.1002/jbm.b.30975
14. Tan JY, Chua CK, Leong KF (2010) Indirect fabrication of gelatin scaffolds using rapid prototyping technology. Virtual Phys Prototyp 5(1):45–53. https://doi.org/10.1080/17452751003759144
15. Liu MJ, Chou SM, Chua CK, Tay BC, Ng BK (2013) The development of silk fibroin scaffolds using an indirect rapid prototyping approach: morphological analysis and cell growth monitoring by spectral-domain optical coherence tomography. Med Eng Phys 35(2):253–262. https://doi.org/10.1016/j.medengphy.2011.09.029
16. Chen CH, Liu J, Chua C-K, Chou S-M, Shyu V, Chen J-P (2014) Cartilage tissue engineering with silk fibroin scaffolds fabricated by indirect additive manufacturing technology. Materials 7(3):2104
17. Yan LP, Oliveira JM, Oliveira AL, Reis RL (2017) Core-shell silk hydrogels with spatially tuned conformations as drug-delivery system. J Tissue Eng Regen Med 11(11):3168–3177. https://doi.org/10.1002/term.2226
18. Yan LP, Silva-Correia J, Ribeiro VP, Miranda-Goncalves V, Correia C, da Silva Morais A, Sousa RA, Reis RM, Oliveira AL, Oliveira JM, Reis RL (2016) Tumor growth suppression induced by biomimetic silk fibroin hydrogels. Sci Rep 6:31037. https://doi.org/10.1038/srep31037
19. Buckland DM, Sadoghi P, Wimmer MD, Vavken P, Pagenstert GI, Valderrabano V, Rosso C (2015) Meta-analysis on biomechanical properties of meniscus repairs: are devices better than sutures?

Knee Surg Sports Traumatol Arthrosc 23(1):83–89. https://doi.org/10.1007/s00167-014-2966-9

20. Pina S, Vieira SI, Rego P, Torres PM, da Cruz e Silva OA, da Cruz e Silva EF, Ferreira JM (2010) Biological responses of brushite-forming Zn- and ZnSr- substituted beta-tricalcium phosphate bone cements. Eur Cells Mater 20:162–177

21. Pina S, Canadas RF, Jimenez G, Peran M, Marchal JA, Reis RL, Oliveira JM (2017) Biofunctional ionic-doped calcium phosphates: silk fibroin composites for bone tissue engineering scaffolding. Cells Tissues Org 204(3–4):150–163. https://doi.org/10.1159/000469703

22. Gruchenberg K, Ignatius A, Friemert B, von Lubken F, Skaer N, Gellynck K, Kessler O, Durselen L (2015) In vivo performance of a novel silk fibroin scaffold for partial meniscal replacement in a sheep model. Knee Surg Sports Traumatol Arthrosc 23(8):2218–2229. https://doi.org/10.1007/s00167-014-3009-2

23. Wojtyla S, Klama P, Baran T (2017) Is 3D printing safe? Analysis of the thermal treatment of thermoplastics: ABS, PLA, PET, and nylon. J Occup Environ Hyg 14(6):D80–d85. https://doi.org/10.1080/15459624.2017.1285489

24. Tas AC (2000) Synthesis of biomimetic Ca-hydroxyapatite powders at 37 degrees C in synthetic body fluids. Biomaterials 21(14):1429–1438

25. Yan LP, Silva-Correia J, Oliveira MB, Vilela C, Pereira H, Sousa RA, Mano JF, Oliveira AL, Oliveira JM, Reis RL (2015) Bilayered silk/silk-nanoCaP scaffolds for osteochondral tissue engineering: in vitro and in vivo assessment of biological performance. Acta Biomater 12:227–241. https://doi.org/10.1016/j.actbio.2014.10.021

26. Beaufils P, Becker R, Kopf S, Matthieu O, Pujol N (2017) The knee meniscus: management of traumatic tears and degenerative lesions. EFORT Open Rev 2(5):195–203. https://doi.org/10.1302/2058-5241.2.160056

27. Vrancken ACT, Buma P, van Tienen TG (2013) Synthetic meniscus replacement: a review. Int Orthop 37(2):291–299. https://doi.org/10.1007/s00264-012-1682-7

28. Hendrikx S, Kascholke C, Flath T, Schumann D, Gressenbuch M, Schulze FP, Hacker MC, Schulz-Siegmund M (2016) Indirect rapid prototyping of sol-gel hybrid glass scaffolds for bone regeneration – effects of organic crosslinker valence, content and molecular weight on mechanical properties. Acta Biomater 35:318–329. https://doi.org/10.1016/j.actbio.2016.02.038

29. Ahmad SN, Hashim J, Ghazali MI (2005) The effects of porosity on mechanical properties of cast discontinuous reinforced metal-matrix composite. J Compos Mater 39(5):451–466. https://doi.org/10.1177/0021998305047096

30. Annabi N, Nichol JW, Zhong X, Ji C, Koshy S, Khademhosseini A, Dehghani F (2010) Controlling the porosity and microarchitecture of hydrogels for tissue engineering. Tissue Eng Part B Rev 16(4):371–383. https://doi.org/10.1089/ten.TEB.2009.0639

31. Wu X, Black L, Santacana-Laffitte G, Patrick CW Jr (2007) Preparation and assessment of glutaraldehyde-crosslinked collagen-chitosan hydrogels for adipose tissue engineering. J Biomed Mater Res Part A 81(1):59–65. https://doi.org/10.1002/jbm.a.31003

32. Loh QL, Choong C (2013) Three-dimensional scaffolds for tissue engineering applications: role of porosity and pore size. Tissue Eng Part B Rev 19(6):485–502. https://doi.org/10.1089/ten.TEB.2012.0437

33. Critchley SE, Kelly DJ (2017) Bioinks for bioprinting functional meniscus and articular cartilage. J 3D Print Med 1(4):269–290. https://doi.org/10.2217/3dp-2017-0012

34. Zhang H, Zhou L, Zhang W (2014) Control of scaffold degradation in tissue engineering: a review. Tissue Eng Part B Rev 20(5):492–502. https://doi.org/10.1089/ten.TEB.2013.0452

35. Brown J, Lu CL, Coburn J, Kaplan DL (2015) Impact of silk biomaterial structure on proteolysis. Acta Biomater 11:212–221. https://doi.org/10.1016/j.actbio.2014.09.013

36. Ghanaati S, Orth C, Unger RE, Barbeck M, Webber MJ, Motta A, Migliaresi C, James Kirkpatrick C (2010) Fine-tuning scaffolds for tissue regeneration: effects of formic acid processing on tissue reaction to silk fibroin. J Tissue Eng Regen Med 4(6):464–472. https://doi.org/10.1002/term.257

37. Cao Y, Wang B (2009) Biodegradation of silk biomaterials. Int J Mol Sci 10(4):1514–1524. https://doi.org/10.3390/ijms10041514

38. Wang Y, Rudym DD, Walsh A, Abrahamsen L, Kim HJ, Kim HS, Kirker-Head C, Kaplan DL (2008) In vivo degradation of three-dimensional silk fibroin scaffolds. Biomaterials 29(24–25):3415–3428. https://doi.org/10.1016/j.biomaterials.2008.05.002

39. Kim UJ, Park J, Joo Kim H, Wada M, Kaplan DL (2005) Three-dimensional aqueous-derived biomaterial scaffolds from silk fibroin. Biomaterials 26(15):2775–2785. https://doi.org/10.1016/j.biomaterials.2004.07.044

40. Ribeiro VP, Pina S, Costa JB, Cengiz IF, García-Fernández L, Fernández-Gutiérrez MdM, Paiva OC, Oliveira AL, San-Román J, Oliveira JM, Reis RL (2019) Enzymatically cross-linked silk fibroin-based hierarchical scaffolds for osteochondral regeneration. ACS Appl Mater Interfaces 11(4):3781–3799. https://doi.org/10.1021/acsami.8b21259

41. Ribeiro VP, da Silva Morais A, Maia FR, Canadas RF, Costa JB, Oliveira AL, Oliveira JM, Reis RL (2018) Combinatory approach for developing silk fibroin scaffolds for cartilage regeneration. Acta Biomater 72:167–181. https://doi.org/10.1016/j.actbio.2018.03.047

42. Abdelgaied A, Stanley M, Galfe M, Berry H, Ingham E, Fisher J (2015) Comparison of the biomechanical tensile and compressive properties of decellularised and natural porcine meniscus. J Biomech 48(8):1389–1396. https://doi.org/10.1016/j.jbiomech.2015.02.044

43. Shriram D, Praveen Kumar G, Cui F, Lee YHD, Subburaj K (2017) Evaluating the effects of material properties of artificial meniscal implant in the human knee joint using finite element analysis. Sci Rep 7(1):6011. https://doi.org/10.1038/s41598-017-06271-3

44. Lee JH, Kisiday J, Grodzinsky AJ (2003) Tissue-engineered versus native cartilage: linkage between cellular mechano-transduction and biomechanical properties. In: Novartis foundation symposium 249:52–64; discussion 64–59, 170–174, 239–141

45. Pereira H, Caridade SG, Frias AM, Silva-Correia J, Pereira DR, Cengiz IF, Mano JF, Oliveira JM, Espregueira-Mendes J, Reis RL (2014) Biomechanical and cellular segmental characterization of human meniscus: building the basis for tissue engineering therapies. Osteoarthr Cartil 22(9):1271–1281. https://doi.org/10.1016/j.joca.2014.07.001

46. Bursac P, Arnoczky S, York A (2009) Dynamic compressive behavior of human meniscus correlates with its extra-cellular matrix composition. Biorheology 46(3):227–237. https://doi.org/10.3233/bir-2009-0537

47. Chia HN, Hull ML (2008) Compressive moduli of the human medial meniscus in the axial and radial directions at equilibrium and at a physiological strain rate. J Orthop Res 26(7):951–956. https://doi.org/10.1002/jor.20573

48. Mandal BB, Park S-H, Gil ES, Kaplan DL (2011) Multilayered silk scaffolds for meniscus tissue engineering. Biomaterials 32(2):639–651. https://doi.org/10.1016/j.biomaterials.2010.08.115

49. Nazarov R, Jin H-J, Kaplan DL (2004) Porous 3-D scaffolds from regenerated silk fibroin. Biomacromol 5(3):718–726. https://doi.org/10.1021/bm034327e

50. Stoffel M, Weichert D, Müller-Rath R (2008) Mechanical modelling and experimental validation of meniscus replacement

material. PAMM 8(1):10197–10198. https://doi.org/10.1002/pamm.200810197

51. Bose S, Fielding G, Tarafder S, Bandyopadhyay A (2013) Understanding of dopant-induced osteogenesis and angiogenesis in calcium phosphate ceramics. Trends Biotechnol 31(10):594–605. https://doi.org/10.1016/j.tibtech.2013.06.005

52. Vepari C, Kaplan DL (2007) Silk as a biomaterial. Prog Polym Sci 32(8–9):991–1007. https://doi.org/10.1016/j.progpolymsci.2007.05.013

53. Yao D, Liu H, Fan Y (2016) Silk scaffolds for musculoskeletal tissue engineering. Exp Biol Med 241(3):238–245. https://doi.org/10.1177/1535370215606994

54. Samavedi S, Whittington AR, Goldstein AS (2013) Calcium phosphate ceramics in bone tissue engineering: a review of properties and their influence on cell behavior. Acta Biomater 9(9):8037–8045. https://doi.org/10.1016/j.actbio.2013.06.014

55. Zhang Y, Wu C, Friis T, Xiao Y (2010) The osteogenic properties of CaP/silk composite scaffolds. Biomaterials 31(10):2848–2856. https://doi.org/10.1016/j.biomaterials.2009.12.049

56. Mandal BB, Gil ES, Panilaitis B, Kaplan DL (2013) Laminar silk scaffolds for aligned tissue fabrication. Macromol Biosci 13(1):48–58. https://doi.org/10.1002/mabi.201200230

57. Xie H, Wang J, He Y, Gu Z, Xu J, Li L, Ye Q (2017) Biocompatibility and safety evaluation of a silk fibroin-doped calcium polyphosphate scaffold copolymer in vitro and in vivo. RSC Adv 7(73):46036–46044. https://doi.org/10.1039/C7RA04999D

58. Kundu B, Rajkhowa R, Kundu SC, Wang X (2013) Silk fibroin biomaterials for tissue regenerations. Adv Drug Deliv Rev 65(4):457–470. https://doi.org/10.1016/j.addr.2012.09.043